

Annual and Semiannual Cycle of Equatorial Atlantic Circulation Associated with Basin-Mode Resonance

PETER BRANDT,^{a,b} MARTIN CLAUS,^a RICHARD J. GREATBATCH,^{a,b} ROBERT KOPTE,^a JOHN M. TOOLE,^c WILLIAM E. JOHNS,^d AND CLAUS W. BÖNING^{a,b}

^a *GEOMAR Helmholtz-Zentrum für Ozeanforschung Kiel, Kiel, Germany*

^b *Christian-Albrechts-Universität zu Kiel, Kiel, Germany*

^c *Woods Hole Oceanographic Institution, Woods Hole, Massachusetts*

^d *Rosenstiel School of Marine and Atmospheric Science/Meteorology and Physical Oceanography, University of Miami, Miami, Florida*

(Manuscript received 16 December 2015, in final form 22 June 2016)

ABSTRACT

Seasonal variability of the tropical Atlantic circulation is dominated by the annual cycle, but semiannual variability is also pronounced, despite weak forcing at that period. This study uses multiyear, full-depth velocity measurements from the central equatorial Atlantic to analyze the vertical structure of annual and semiannual variations of zonal velocity. A baroclinic modal decomposition finds that the annual cycle is dominated by the fourth mode and the semiannual cycle is dominated by the second mode. Similar local behavior is found in a high-resolution general circulation model. This simulation reveals that the annual and semiannual cycles of the respective dominant baroclinic modes are associated with characteristic basinwide structures. Using an idealized, linear, reduced-gravity model to simulate the dynamics of individual baroclinic modes, it is shown that the observed circulation variability can be explained by resonant equatorial basin modes. Corollary simulations of the reduced-gravity model with varying basin geometry (i.e., square basin vs realistic coastlines) or forcing (i.e., spatially uniform vs spatially variable wind) show a structural robustness of the simulated basin modes. A main focus of this study is the seasonal variability of the Equatorial Undercurrent (EUC) as identified in recent observational studies. Main characteristics of the observed EUC including seasonal variability of transport, core depth, and maximum core velocity can be explained by the linear superposition of the dominant equatorial basin modes as obtained from the reduced-gravity model.

1. Introduction

The mean tropical Atlantic circulation manifests a superposition of the wind-driven and thermohaline circulations that are focused in the upper ocean and near the western boundary (Schott et al. 2004; Schott et al. 2005). At the equator, below the surface wind drift associated with the equatorial easterlies, the Equatorial Undercurrent (EUC) flows eastward along the equator, contributing to the Atlantic meridional overturning circulation and to the wind-driven subtropical cells

(Hazeleger and de Vries 2003; Hazeleger et al. 2003). The EUC is among the strongest currents in the tropical Atlantic and flows down the depth-dependent eastward pressure gradient. While nonlinearities contribute to its mean characteristics (Charney 1960; Qiao and Weisberg 1997), the EUC is essentially governed by linear dynamics with the meridional momentum equation being approximated by the geostrophic balance (Stommel 1960; McCreary 1981).

The main focus of the present study is the seasonal cycle of the zonal velocity that is the dominant variability in the upper layer of the central equatorial Atlantic, particularly modulating the mean eastward flow of the EUC. A question to be addressed is whether the flow variations can be understood as a linear wave response to annual and semiannual wind forcing. Using a general circulation model (GCM), Philander and Pacanowski (1986) found that the western part of the equatorial Atlantic is dominated by a local response to

 Denotes Open Access content.

Corresponding author address: Peter Brandt, GEOMAR Helmholtz-Zentrum für Ozeanforschung Kiel, Düsterbrook Weg 20, 24105 Kiel, Germany.
E-mail: pbrandt@geomar.de

DOI: 10.1175/JPO-D-15-0248.1

the annual wind forcing, while the central and eastern Atlantic shows a stronger semiannual cycle only partially attributable to the local wind forcing. The downward propagation of energy supplied by periodic wind forcing at the sea surface can be conceptually described by equatorial beams. Eastward- and westward-propagating beams are found analytically as the sum of low-order baroclinic mode equatorial Kelvin and Rossby waves, respectively (McCreary 1984). In the tropical Atlantic, such beams are most pronounced at the annual period; the associated upward phase propagation can be identified in direct current observations as well as in high-resolution GCM simulations (Brandt and Eden 2005). In relation to the relative strength of the annual and semiannual wind forcing of the tropical Atlantic, the semiannual cycle of the velocity field is enhanced compared to the annual cycle. Using idealized and realistic simulations of the tropical Atlantic, Thierry et al. (2004) found that the propagation of second baroclinic mode equatorial Kelvin and long Rossby waves is in resonance with the semiannual wind forcing. Because of the downward energy propagation and the generally dissipative character of the basin resonance, bottom reflections or the presence of the Mid-Atlantic Ridge do not appear to affect the general structure of the semiannual cycle of the velocity field. The spatial and temporal structure of such resonance phenomena are best described by equatorial basin modes (Cane and Moore 1981). These modes are low-frequency standing equatorial modes composed of equatorial Kelvin and long Rossby waves in the context of a shallow-water model with a given gravity wave speed characteristic of a specific baroclinic mode. The total travel time of both types of waves across the basin defines the period of the gravest basin mode. In the inviscid case, the analytical solution by Cane and Moore (1981) has a singularity in the midbasin due to Rossby wave focusing. The introduction of lateral diffusion and/or mean flow can prevent such focusing, which makes solutions more realistic in comparison to observations (Greatbatch et al. 2012; Claus et al. 2014).

The concept of equatorial basin modes has been applied to explain the dynamics of observed intraseasonal, seasonal, and interannual variability in the three equatorial basins (see, e.g., Johnson and Zhang 2003; Fu 2007; Ding et al. 2009). At the semiannual time scale, variability in both the Atlantic and Indian Oceans appears consistent with a resonance of the second baroclinic mode that can be approximated by an equatorial basin mode (Jensen 1993; Han et al. 1999; Thierry et al. 2004; Ding et al. 2009). A subsequent study of basin-mode resonance in the Indian Ocean by Han et al. (2011) highlighted the influence of wave damping and

the shape of the equatorial basin on the spatial structure of these modes, while the existence of equatorial basin modes was found to be a robust feature in simulations with models of different complexity.

In the present paper, we explore the role of the gravest equatorial basin modes of different baroclinic modes in shaping the seasonal cycle of equatorial Atlantic zonal velocity with a particular focus on the EUC. While a basin-mode description of semiannual variability was discussed in previous studies, we will show evidence of a resonant basin mode at the fourth baroclinic mode, annual period.

During the recent decade, an enhanced equatorial observing system consisting of subsurface current meter moorings deployed in cross-equatorial arrays at different longitudes, that is, 23°W, 10°W, and 0°, has been maintained, and the resulting data has been used to document the seasonal behavior of the Atlantic EUC (Brandt et al. 2014; Johns et al. 2014). Some of the identified characteristics, such as the annual cycle of EUC deepening and shallowing and the semiannual cycle of EUC core velocity, have not been dynamically explained so far. Here, we use full-depth velocity observations taken at the equator, 23°W, to analyze the vertical structure of the seasonal cycle. Further, we compare these results to simulations with a primitive equation numerical model that reveals the horizontal structure of the dominant baroclinic modes in a realistic setting. The obtained horizontal structure resembles that of equatorial basin modes as simulated with a reduced-gravity model. The gravest equatorial basin modes have their strongest zonal velocity oscillations on the equator in midbasin and might thus be well sampled by the 23°W moored observations. The reduced-gravity model is further used to study the structural dependence of the basin modes on the basin geometry (i.e., square basin vs realistic coastlines) and forcing (i.e., spatially uniform vs realistic wind forcing). The skill of the linear reduced-gravity model in replicating the dominant features of the seasonal cycle of the zonal velocity in the equatorial Atlantic demonstrates that a large part of the seasonal variability may be explained by equatorial wave dynamics associated with just two equatorial basin modes.

The layout of the paper is as follows: In section 2, the moored velocity and shipboard conductivity–temperature–depth (CTD) data are introduced. The model hierarchy, composed of a GCM in a realistic setting and an idealized reduced-gravity model applied for different levels of complexity, is described in section 4. The results section includes a characterization of the annual and semiannual variations as obtained from the mooring data and from the GCM (section 4a), a comparison between the

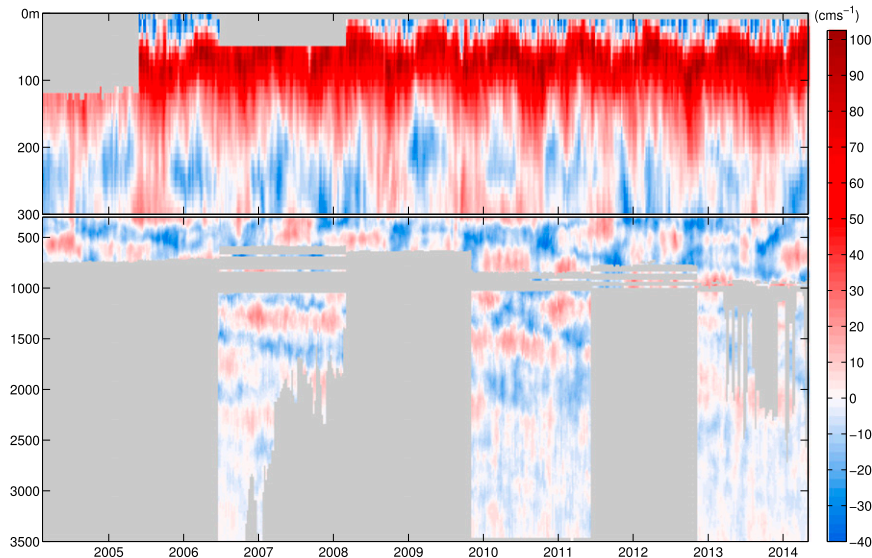


FIG. 1. Observed zonal velocity from the equator, 23°W, and above 3500-m depth. Velocity data above about 600 m are from moored acoustic Doppler current profilers; those between 600 and 1000 m are from single-point current meters, and those below 1000 m are from moored profilers. The gray areas mark depths not sampled by the deployed instrumentation. The upper 300 m are enlarged compared to the deeper part of the time series.

GCM simulation and the idealized reduced-gravity simulations fitted to moored velocity data from the equator at 23°W (section 4b), and an analysis of the variability of the EUC and its dependence on resonant equatorial basin modes (section 4c). Summary and discussion are presented in section 5.

2. Mooring and CTD data

The zonal velocity observations were obtained from current meter moorings deployed at the equator, 23°W, from February 2004 to April 2014 (Fig. 1). This dataset represents an update of that published by Brandt et al. (2011, 2012). Here, we use mooring data from seven successive deployment periods of approximately 1.5-yr duration. The moorings were equipped with two ADCPs. The upper one was a 300- or a 150-kHz ADCP installed at 100- to 230-m depth and profiled upward from just below the EUC. The lower instrument was a 75-kHz ADCP that either profiled downward from just beneath the upper instrument or upward from about 600- to 650-m depth. We applied a 40-h, low-pass filter to hourly interpolated current data (ADCP sampling rates varied typically between 0.5 and 1 h⁻¹, but it was set to about 3 samples per day during one mooring period) to eliminate tidal currents, and the detided data were subsequently subsampled to 12-hourly resolution. Between 600 and 1000 m during several mooring periods, a few single-point current meters of a different type were installed.

Deeper in the water column, a McLane Moored Profiler (MMP) was programmed to sample the depth range between 1000 and 3500 m. The installed profilers acquired data during three of the seven mooring periods, with a somewhat reduced measurement range during the third and seventh mooring periods (see Fig. 1). The MMPs were programmed to occupy profiles in bursts of two one-way traverses every 4 or 6 days, with the one-way profiles initiated 6 h apart. No temporal filter was applied to the acquired velocity data. Given the length of the time series, the impact of measurement noise on the derived amplitude of the annual and semiannual cycles can be regarded as negligible.

The time series has so far been used to study equatorial deep jets (EDJs) that are visible as bands of eastward and westward velocity characterized by downward phase propagation and a periodicity of about 4.5 yr (Brandt et al. 2011) as well as the seasonal and interannual variability of the EUC (Brandt et al. 2014). Here, we further exploit the data to study the seasonal circulation variability taking particular advantage of the nearly full-depth velocity measurements to decompose the velocity field according to baroclinic modes at selected frequencies.

For the decomposition of the moored velocity data into baroclinic modes, we used vertical structure functions for a flat bottom derived from a mean Brunt–Väisälä frequency profile that was obtained by averaging individual Brunt–Väisälä frequency profiles calculated from shipboard CTD measurements taken during the

TABLE 1. Characteristics of the baroclinic modal decomposition using a mean Brunt–Väisälä frequency profile derived from CTD casts during mooring service cruises. The gravest basin mode period ($4L/c$) is calculated for a width of $L = 5.8 \times 10^6$ m $\sim 52.8^\circ$ (i.e., the width of the rectangular basin).

Baroclinic mode	Phase velocity, c (m s^{-1})	Gravest basin-mode period (days)	Depth of first zero-crossing (m)	Depth of second zero-crossing (m)
1	2.47	109	1410	—
2	1.32	203	295	2220
3	0.95	284	85	795
4	0.74	361	65	400
5	0.57	473	50	270

mooring service cruises. The structure functions of the low baroclinic modes change only marginally when taking into account the variability about the mean Brunt–Väisälä frequency profile; however, some variations in the depth of zero-crossings of the profiles result when considering different ocean depths. To have a consistent analysis regarding the vertical structure of observed and simulated velocity variability, we decided to use one set of structure functions derived from the observed mean Brunt–Väisälä frequency profile for a water depth of 4500 m for both the analysis of the zonal velocity from moored observations as well as from the GCM. The main characteristics of the baroclinic modes are given in Table 1; the two modes of particular interest in the present study, that is, the second and fourth baroclinic mode, together with the mean zonal velocity in the upper 300 m derived from the moored time series are presented in Fig. 2.

3. Model simulations

The GCM builds on a global configuration [Tropical Atlantic Nest at $1/10^\circ$ (TRATL01)] of the Nucleus for European Modeling of the Ocean (NEMO) code (Madec 2008) in which the grid resolution of 0.5° is refined to 0.1° in the Atlantic Ocean between 30°N and 30°S via two-way nesting (Debreu and Blayo 2008). It includes 46 vertical levels, with increasing thickness from 6 m at the surface to 250 m at depth. With an interannually varying forcing given by the Co-ordinated Ocean–Ice Reference Experiments (CORE; Griffies et al. 2009) reanalysis data over the period 1948–2007, the TRATL01 configuration was used by Duteil et al. (2014) to study the circulation mechanisms responsible for the ventilation of the oxygen minimum zone in the eastern tropical Atlantic. A particular finding of that study was the improved realism of the equatorial current system, owing to the higher resolution of the TRATL01 model compared to a 0.5° resolution model. Here, we use the output from the TRATL01 simulation over the period 1995–2007, as well as 3-yr subsets of the

time series, to assess the strength of the interannual variability that might be present in the moored observations covering periods of at least 3 yr at the different longitudes. We compare the results of the TRATL01 simulations with observational results that are based on current meter moorings along meridional sections at 23°W , 10°W , and 0° , deployed from October 2007 to June 2011 (Johns et al. 2014). The comparison focuses on the mean and the seasonal cycle of the EUC transport (Fig. 3). As the time period of the TRATL01 simulation and the observations only marginally overlap, we examined the stability of the mean EUC seasonal cycle for different time periods using the dataset of the ECMWF Ocean Reanalysis System 4 (Balmaseda et al. 2013). We found that in the reanalysis, the mean seasonal cycle of the EUC for 1995–2007 is similar in amplitude and phase to that of 2007–11, justifying our comparison of TRATL01 simulations with observations from different periods.

The moored data show that at 23°W , the strongest EUC transport is found in boreal autumn during the period of maximum easterly wind stress that varies dominantly at annual period. At 10°W , the EUC transport shows a semiannual cycle with maxima in boreal spring and autumn. Farther to the east, the wind forcing is dominated by its semiannual component. However, the observed EUC transport at 0° has only a single maximum in boreal spring. The comparison of simulated and observed EUC transports (Fig. 3) shows that (i) the model’s annual-mean EUC transport is generally overestimated and decreases more with distance from west to east as compared to observations (the interannual variability, delineated by the successive 3-yr subsets of the time series, is not able to account for these differences); (ii) within the seasonal cycle, the timing of the boreal autumn maximum in the EUC transport is well represented at 23° and 10°W ; and (iii) there is only a weak simulated seasonal cycle at 0° with the observed boreal spring maximum not represented. At 23°W , the simulation is found to capture the main characteristics of the seasonal velocity variability observed on the

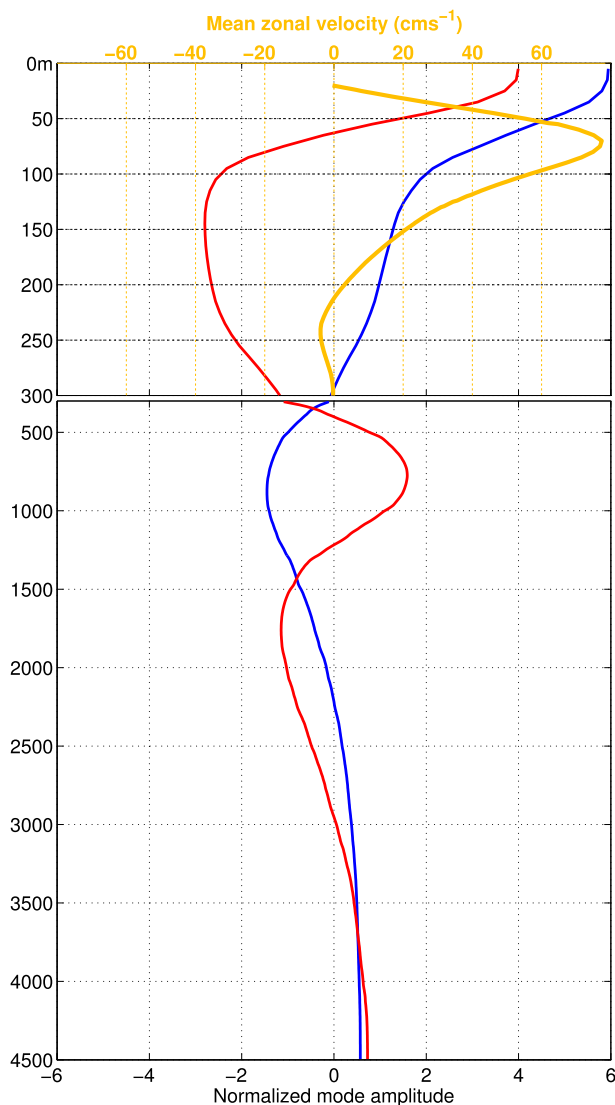


FIG. 2. Normalized vertical structure function of the second (blue) and fourth (red) baroclinic mode as derived from a mean Brunt–Väisälä frequency profile from the equator, 23°W. Normalization is performed with regard to the standard deviation of the structure functions. In the enlarged upper 300-m depth range the mean zonal velocity (yellow) is also shown.

equator, including the amplitude and phase of the annual harmonic of zonal velocity (Fig. 4) and the spectral behavior (Fig. 5). In particular, the reasonable representation of the observed seasonal cycle of zonal velocity in the central equatorial Atlantic, that is, close to midbasin where velocity oscillations of the gravest equatorial basin mode are strongest (Cane and Moore 1981), encourages us to focus on a baroclinic modal decomposition analysis at the annual and semiannual period.

To further the dynamical understanding, we consider single baroclinic mode solutions by applying a linear

reduced-gravity model in spherical coordinates. For governing equations and further details of the model, see Greatbatch et al. (2012). The internal gravity wave speeds of the reduced-gravity model are taken from the baroclinic modal decomposition of the observed mean Brunt–Väisälä frequency profile described above (Table 1). The lateral eddy viscosity is set to $300 \text{ m}^2 \text{ s}^{-1}$, which yields the most realistic results with regard to the meridional structure of high baroclinic mode waves (Greatbatch et al. 2012; Claus et al. 2014). However, model simulations with reduced eddy viscosity, that is, $100 \text{ m}^2 \text{ s}^{-1}$, give similar results. The governing equations are applied to a rectangular as well as a realistic coastline domain with northern and southern boundaries at 20°N/S, respectively. Sponge layers at the northern and southern boundaries prevent Kelvin wave propagation along those boundaries. The latitudes of the northern and southern boundaries in the reduced-gravity model are chosen to be far enough away from the equator to have little influence on the structure of the simulated equatorial basin modes. The horizontal resolution is the same as that used in the GCM ($1/10^\circ$ in both longitude and latitude).

Periodic wind stress forcing is applied to the momentum equations (either annually or semiannually), and all simulations with the reduced-gravity model are run for 100 yr in order to obtain a stable, periodically oscillating solution. We note that the resulting oscillation amplitude will depend on different aspects of the model configuration, including the applied damping, the basin geometry, the strength of the basin mode resonance, and, most importantly, the projection of the wind forcing onto the different baroclinic modes. Here, we use similar wind coupling coefficients as, for example, in Shankar et al. (1996) or Han et al. (1999). However, the annual and semiannual oscillation amplitudes derived from the linear reduced-gravity model are scaled using the ratio of observed and simulated amplitudes of the annual and semiannual oscillations on the equator at 23°W. This adjustment was performed to counter any misrepresentation of damping or forcing in the reduced-gravity model with respect to the simulated oscillation amplitude. The reduced-gravity model is then used to quantify the horizontal structure of the amplitude and phase of the annual and semiannual cycle throughout the tropical Atlantic.

Three sets of reduced-gravity model simulations are presented. The first uses an idealized rectangular domain with a basin width of 52.8° in longitude forced by spatially uniform zonal wind stress at the annual or semiannual period. The second set of simulations is identical except that the model domain is defined by the observed 1000-m isobath of the equatorial Atlantic

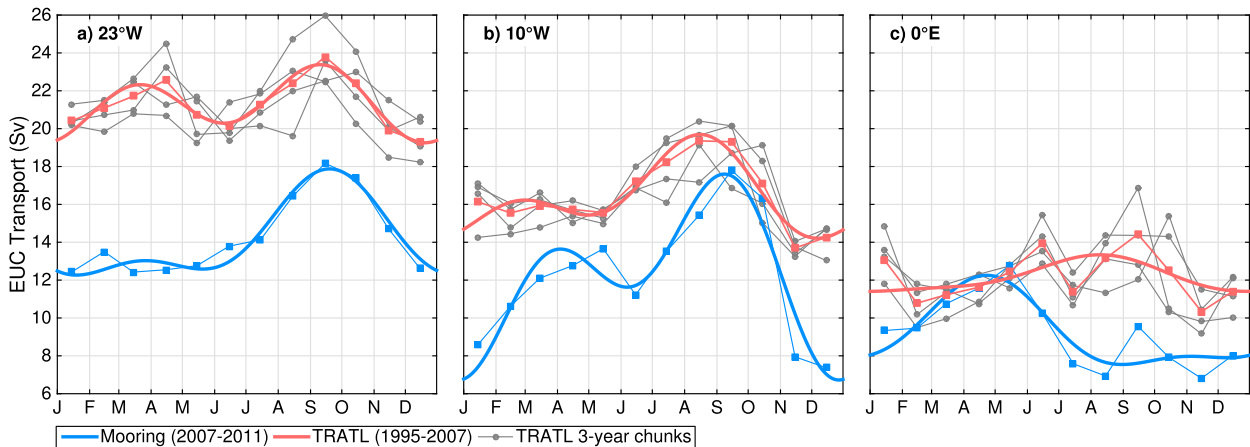


FIG. 3. Monthly means (squares) of the 30–300-m EUC transport at 23°W, 10°W, and 0° from observations taken from October 2007 to June 2011 (Johns et al. 2014, blue) and the TRATL01 model output derived for the whole model period 1995–2007 (red) as well as for four successive 3-yr subsets of the time series (gray). Thick solid lines represent the mean seasonal cycles derived from annual and semiannual harmonic fits of the observations (blue) and simulations (red).

basin at the eastern and western boundaries. Note that we used a slightly different basin width for the rectangular domain from that used by Greatbatch et al. (2012; in that case 55° in longitude) in order to ensure that the resonance periods in the model simulations with a rectangular basin and a basin with realistic coastlines are basically the same. For both sets of simulations having spatially uniform wind forcing, in addition to the amplitude scaling, a spatially uniform phase shift is applied

to the simulated annual and semiannual oscillations over the whole domain to achieve agreement between simulated and observed phases on the equator at 23°W. Following this approach, the adjusted model output is independent of the amplitude and phase of the wind forcing. The third set of simulations is the same as the second (i.e., both sets using realistic coastlines), except that we use a spatially varying, harmonically oscillating wind forcing derived from the NCEP–DOE AMIP-II

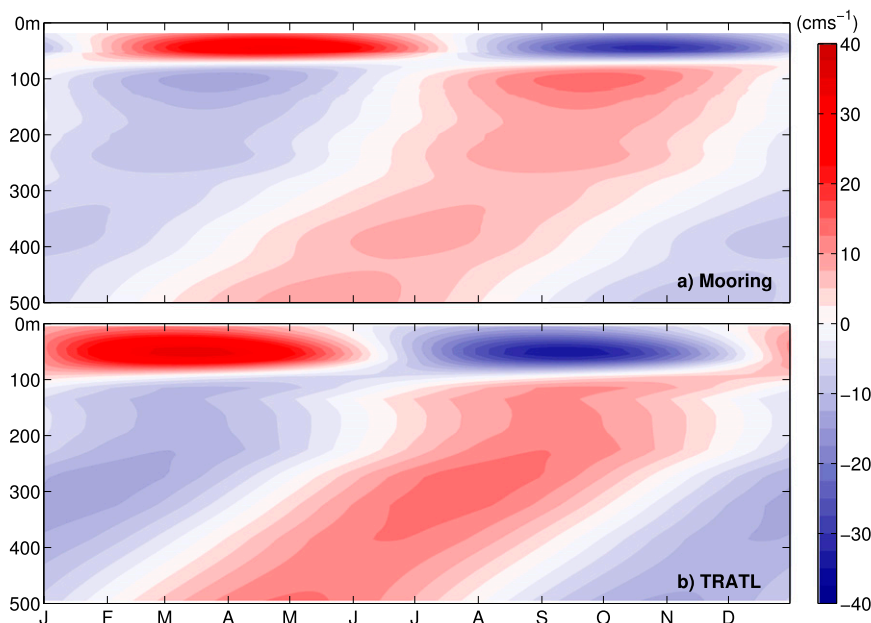


FIG. 4. Annual cycle of zonal velocity (cm s^{-1}) from the equator, 23°W, as reconstructed using only (a) the annual harmonic fit applied to moored velocity data and (b) the TRATL01 model output.

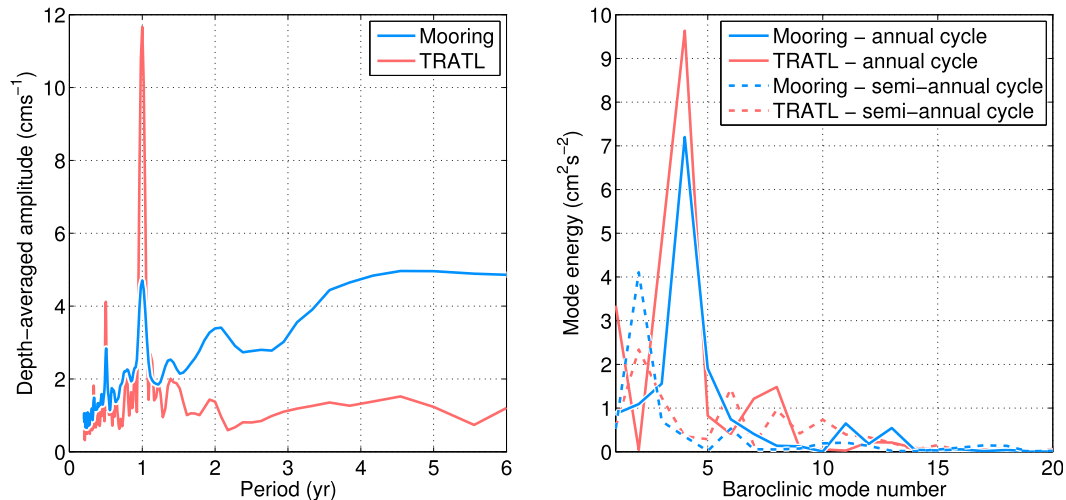


FIG. 5. (left) Frequency spectra of observed zonal velocity from the equator, 23°W, and (right) baroclinic mode spectra of the annual (solid) and semiannual (dashed) cycles derived from the equatorial mooring (blue) and the TRATL01 model (red). The spectra of observed zonal velocity in the left panel were derived by fitting harmonic functions to the available data at each depth level, followed by vertical averaging.

reanalysis product (Kanamitsu et al. 2002). In this third set of simulations, we use zonal and meridional wind forcing. Specifically, the amplitude and phase of the annual and semiannual wind forcing are obtained by harmonic fits at the corresponding periods. In this most realistic set of simulations with the reduced-gravity model, only the amplitudes of simulated velocity oscillations are scaled according to the observed values on the equator at 23°W; no phase adjustment is done, as we expect the phase of the oscillations to be well determined by the applied wind forcing.

4. Results

a. Characteristics of the annual and semiannual cycle

The dominant signals in the zonal velocity field observed at the 23°W equatorial mooring (Fig. 1) are the seasonal cycle and the interannual variations associated with the equatorial deep jets. By analyzing an early subset of the mooring data, Brandt et al. (2006) identified strong annual cycle amplitudes above and below the mean core depth of the EUC that are in phase opposition. Deeper in the water column, sizable annual amplitudes were also found. A reconstruction of the mean annual cycle from a harmonic fit of the moored velocity data (Fig. 4a) shows a clearly visible phase jump at about 70-m depth associated with zero amplitude. Around 100-m depth, another maximum in the annual amplitude is found corresponding to the lower part of the EUC. This pattern represents the upward and downward movement of the EUC velocity core during the year,

being shallowest in boreal spring and deepest in autumn. Below the EUC, upward phase propagation is evident that is, according to linear equatorial wave theory, associated with downward energy propagation. The simulation with the TRATL01 model (Fig. 4b) shows a very similar behavior. Main differences compared to the observations are the slightly deeper depth of the phase jump and the larger amplitude (with a maximum at about 300 m) below the EUC core. Note that the depth of maximum eastward velocity of the annual-mean EUC at 23°W is about 70 m in the observations and about 85 m in the TRATL01 simulation, which following McCreary (1981) is indicative of too large vertical diffusion in the TRATL01 simulation.

To derive a frequency spectrum from the irregularly sampled moored velocity dataset, we performed harmonic fits of the available data at each depth and averaged the derived amplitude vertically over the whole depth range (Fig. 5a). The obtained spectrum clearly shows distinct peaks at annual and semiannual periods with another weaker peak at about 120 days. The broad amplitude maximum at the 4–5-yr period is associated with the EDJs (Brandt et al. 2011; Ascani et al. 2015). The strong peaks in the zonal velocity amplitude suggest the presence of strong forcing at these periods and/or a resonant behavior or, possibly, indicate influence from flow instabilities (not discussed further here). Similar calculations performed using the TRATL01 model velocity data also reveal spectral peaks at annual, semi-annual, and 120-day periods with the peak at the annual period being substantially stronger by a factor of 2 to 3 compared to observations. Enhanced amplitudes at

interannual time scales are missing in the TRATL01 solution, pointing toward a well-known deficiency of such models in representing the EDJs (Ascani et al. 2015).

To analyze the vertical structure of the annual and semiannual cycle, we performed a baroclinic modal decomposition of the reconstructed annual and semiannual cycles (Fig. 5b) at each discrete time step. The mode energy was then obtained by averaging the square of the derived coefficients over a whole cycle. As expected from previous studies (Thierry et al. 2004; Ding et al. 2009), the semiannual energy density peaks at the second baroclinic mode. More surprising is the strong peak of the annual cycle at the fourth baroclinic mode. The vertical structure function of the fourth baroclinic mode has its first zero-crossing at 65-m depth (Table 1), which is close to the depth of the mean EUC core (Fig. 2). Thus, the phase shift of the annual cycle within the EUC (Fig. 4a) is associated with the dominance of this baroclinic mode. Note the weak annual amplitudes at about 400-m depth (Fig. 4) that correspond to the second zero-crossing of the fourth baroclinic mode (Table 1) suggesting also a significant contribution of that baroclinic mode to the velocity variability below the EUC.

The TRATL01 simulation shows very similar characteristics: The peak of the second baroclinic mode, semiannual cycle, is slightly weaker than observed, and the peak of the fourth baroclinic mode, annual cycle, is slightly stronger (Fig. 5b). We also note that the amplitude of the third/fifth baroclinic mode, annual cycle, is higher/lower in the TRATL01 simulations compared to the observations, which indicate a shift of the simulated annual cycle to lower modes having deeper first zero-crossings compared to higher modes (Table 1). This is consistent with our findings from the comparison of reconstructed annual cycles (Fig. 4), where the phase shift in the annual cycle between the upper and lower part of the EUC is deeper in the simulations compared to the observations.

In a next step, the TRATL01 output (which reproduces the main characteristics of the seasonal velocity variability on the equator at 23°W) is taken to calculate the horizontal pattern associated with the second baroclinic mode, semiannual cycle, and the fourth baroclinic mode, annual cycle (Fig. 6). These patterns reveal (i) an elongated amplitude maximum along the equator in midbasin, (ii) general westward phase propagation off as well as on the equator, and (iii) a meridionally broader pattern of the semiannual cycle relative to the annual cycle. Both patterns have similarities with equatorial basin modes as theoretically described by Cane and Moore (1981) but reveal at the same time an asymmetry with respect to the

equator. We next compare patterns simulated using TRATL01 with idealized simulations using the reduced-gravity model.

b. Equatorial basin modes as simulated with the reduced-gravity model

The reduced-gravity model was next applied to study the resonance behavior of the equatorial ocean forced with spatially uniform zonal forcing of fixed amplitude but different oscillation periods. The simulations were performed for the square basin as well as for the basin with realistic coastlines. Following previous studies (Greatbatch et al. 2012; Claus et al. 2014), we chose the root-mean-square (RMS) of the zonal velocity along the equator calculated in the stable, periodically oscillating state to identify the resonance of the equatorial basin modes (Fig. 7). Here, the estimate is taken over the final complete oscillation cycle. The simulations indicate resonance of the second baroclinic mode near the semiannual period at about 210 days and resonance of the fourth baroclinic mode almost exactly at the annual period. At the resonance periods, the amplitudes of the zonal velocity oscillations are somewhat reduced in the case of a basin with realistic coastlines compared to a square basin. This likely is the result of the slanting western boundary reducing the amplitude of the reflected Kelvin wave in comparison to a straight meridional boundary (Cane and Gent 1984) and possibly also a consequence of the Gulf of Guinea coastline shape in the east. Note that Fig. 7 indicates secondary resonances near 100 days for the second baroclinic mode and near the semiannual period for the fourth baroclinic mode. Several effects that could impact the resonance periods are neglected in the reduced-gravity model. For example, in the real ocean the resonance periods may be reduced in comparison to the idealized simulation presented here due to the presence of a mean flow as shown for equatorial basin modes of higher baroclinic modes (Claus et al. 2014) or due to the nonlinear increase of the propagation speed of equatorial waves (Boyd 1980; Greatbatch 1985).

Different runs with the reduced-gravity model sought to identify the structure of the basin modes in a uniformly forced rectangular ocean and to study the influence of realistic coastlines and wind forcing. Similar to the TRATL01 simulation, the amplitude and phase of the second baroclinic mode, semiannual cycle, and the fourth baroclinic mode, annual cycle, in the reduced-gravity model shows an elongated amplitude maximum along the equator in midbasin and generally westward phase propagation (Figs. 8–10). The solutions of the reduced-gravity model for a square basin and spatially uniform zonal forcing are symmetric with

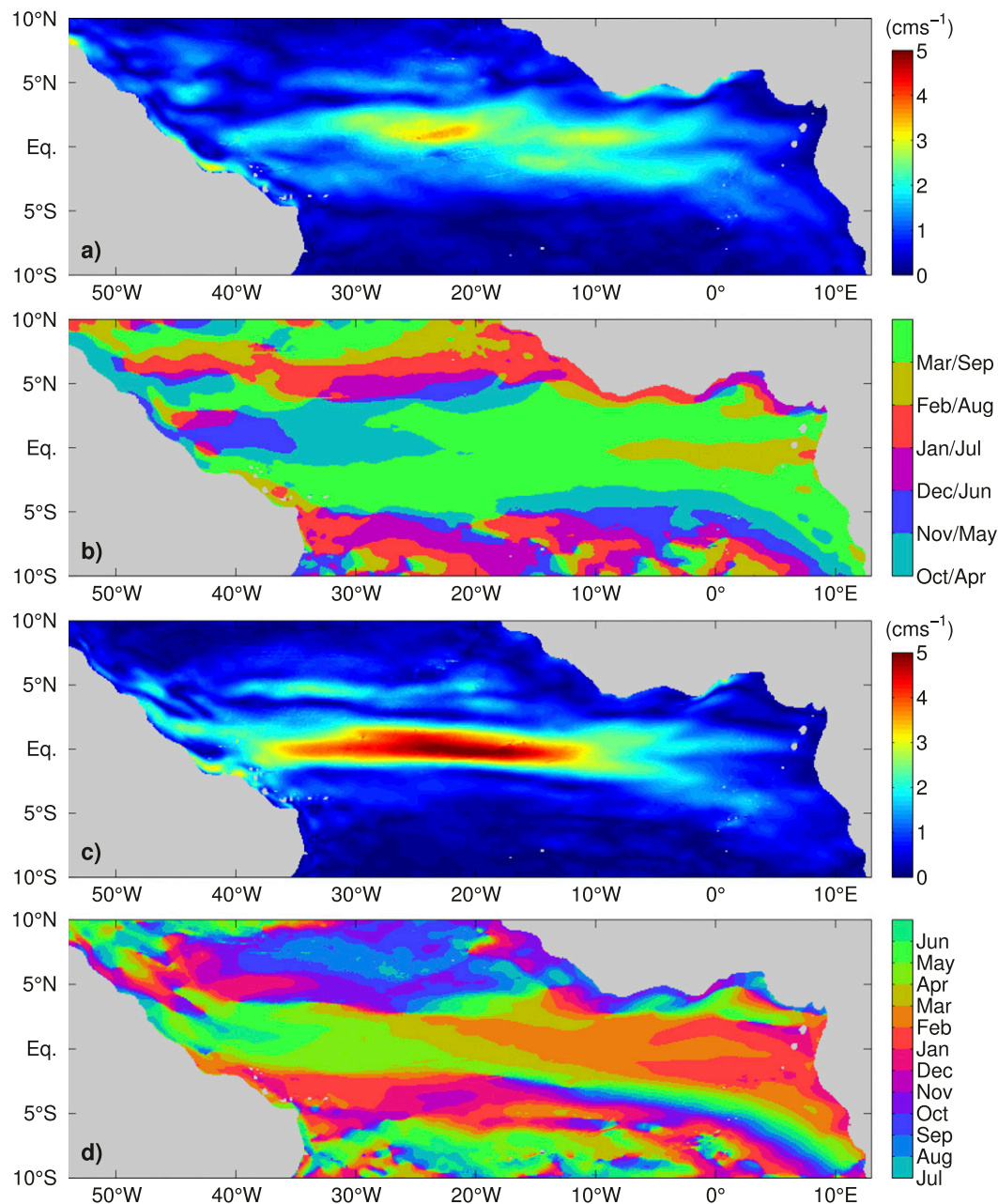


FIG. 6. The (a),(c) amplitude and (b),(d) phase of the (a),(b) second baroclinic mode, semiannual cycle, and of the (c),(d) fourth baroclinic mode, annual cycle, of zonal velocity from the TRATL01 model. To derive the 3D zonal velocity field associated with the specific baroclinic mode, the amplitudes have to be multiplied by the corresponding vertical structure functions shown in Fig. 2. The phase is given in month of the year when maximum eastward velocity occurs at the surface.

respect to the equator. The main difference between the solutions for the second baroclinic mode, semiannual cycle (Figs. 8a,c), and the fourth baroclinic mode, annual cycle (Figs. 8b,d), is the meridionally broader pattern of the second baroclinic mode, semiannual cycle; in the case of the semiannual cycle, regions farther away from the equator are more affected

by the basin mode oscillations than for the annual cycle.

The introduction of realistic coastlines and the associated change of basin geometry induce an asymmetry in the meridional structure of the basin modes; that is, in the western part of the domain, the amplitude maximum is shifted northward, whereas in the east the amplitude

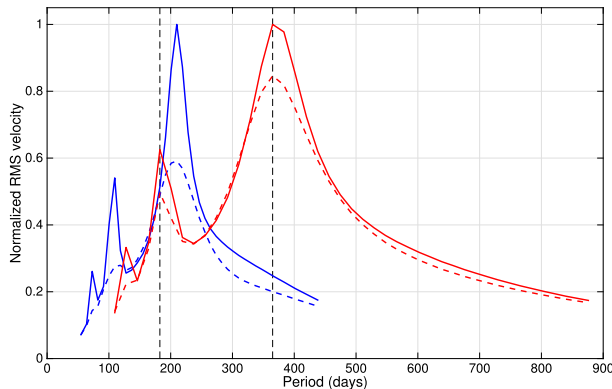


FIG. 7. Normalized RMS of the zonal velocity along the equator calculated for the final complete oscillation cycle as a function of the period of the applied spatially uniform zonal forcing for simulations with the reduced-gravity model. Simulations are performed for the square basin (solid lines) as well as for the basin with realistic coastlines (dashed lines). The velocity in the ordinate for the second (blue) and fourth baroclinic mode (red) simulation is normalized by the maximum RMS of the respective simulations for the square basin. Vertical dashed lines mark the period of the semiannual and annual cycles.

in the southern lobe is enhanced, while that in the northern lobe is reduced. Consistent results were found for the basin mode of the second baroclinic mode, semiannual cycle, using a GCM with realistic basin geometry (Thierry et al. 2004) that showed notable meridional asymmetry in the deeper circulation pattern. Here, the second baroclinic mode, semiannual cycle, is more strongly influenced by the introduction of realistic coastlines compared to the fourth baroclinic mode, annual cycle. This could be expected because of the smaller meridional scale associated with the fourth baroclinic mode compared to the second baroclinic mode. Interesting to note are the amplitude maxima at the northeastern boundary (Figs. 9a,b) that are likely associated with the propagation of coastally trapped waves around the Gulf of Guinea. Somewhat similar maxima are also found in the TRATL01 solution (Fig. 6), especially for the second baroclinic mode, semiannual cycle, case.

A final set of simulations with the reduced-gravity model was performed that used a realistic spatial pattern of annual and semiannual wind forcing. In contrast to the first two sets of simulations that were forced with spatially uniform winds, we only adjusted the amplitude of the simulated basin mode in comparison to the moored observations on the equator at 23°W. The simulated phase was unaltered, as we expect the phase of the oscillations to be well determined by the applied wind forcing. With the more realistic wind forcing, the second baroclinic mode, semiannual cycle, develops two

separate amplitude maxima in space (Fig. 10a): one centered on the equator at about 10°W and the second slightly north of the equator west of 20°W. A similar structure can be found in the TRATL01 simulation (Fig. 6a). When changing from the reduced-gravity model simulations with spatially uniform to realistic wind forcing, the main difference for the fourth baroclinic mode, annual cycle, is a shift in the phase along the equator of up to 2 months, suggesting a deficiency of the reduced-gravity model in the most realistic setup with an unaltered phase. Again, there is good agreement between the linear, reduced-gravity model and the TRATL01 model in this case (Figs. 10b,d and Figs. 6b,d).

Overall, the regular oscillations produced by the reduced-gravity model are suggestive of equatorial basin modes. Realistic coastlines and realistic wind forcing both induce meridional asymmetry in the basin-mode structure, the influence being stronger for the lower baroclinic mode, semiannual cycle, compared to the annual cycle. Confirming previous results using models of different complexity applied to the Indian and Atlantic Oceans (Thierry et al. 2004; Han et al. 2011), our results also show that the general structure of a resonant equatorial basin mode is fairly robust [similar structures are observed in the various reduced-gravity model simulations (Figs. 8–10) as well as the GCM (Fig. 6)].

c. EUC variability associated with equatorial basin modes

A question that arises from the above results is to what extent can the observed seasonal behavior of the EUC be explained by linear equatorial basin modes. Using the basin-mode solutions from the reduced-gravity model, we reconstruct the 3D structure of the velocity anomaly field by applying the vertical structure functions of the corresponding baroclinic modes (Fig. 2). By adding the reconstructed simulated velocity anomalies to the mean velocity from meridional ship-board sections at different longitudes (Johns et al. 2014), we obtain a time series of zonal velocity that can be analyzed in a similar fashion as the observed time series. In particular, EUC transports are calculated following Johns et al. (2014), that is, integrating only eastward velocities within the latitudinal range from 1°12'S to 1°12'N and the depth range from 0 to 300 m. Here, the reconstruction obtained from the reduced-gravity model simulations only includes the velocity variability associated with the second baroclinic mode, semiannual cycle, and the fourth baroclinic mode, annual cycle, and is derived for all three cases: the square basin, realistic geometry, and realistic wind forcing.

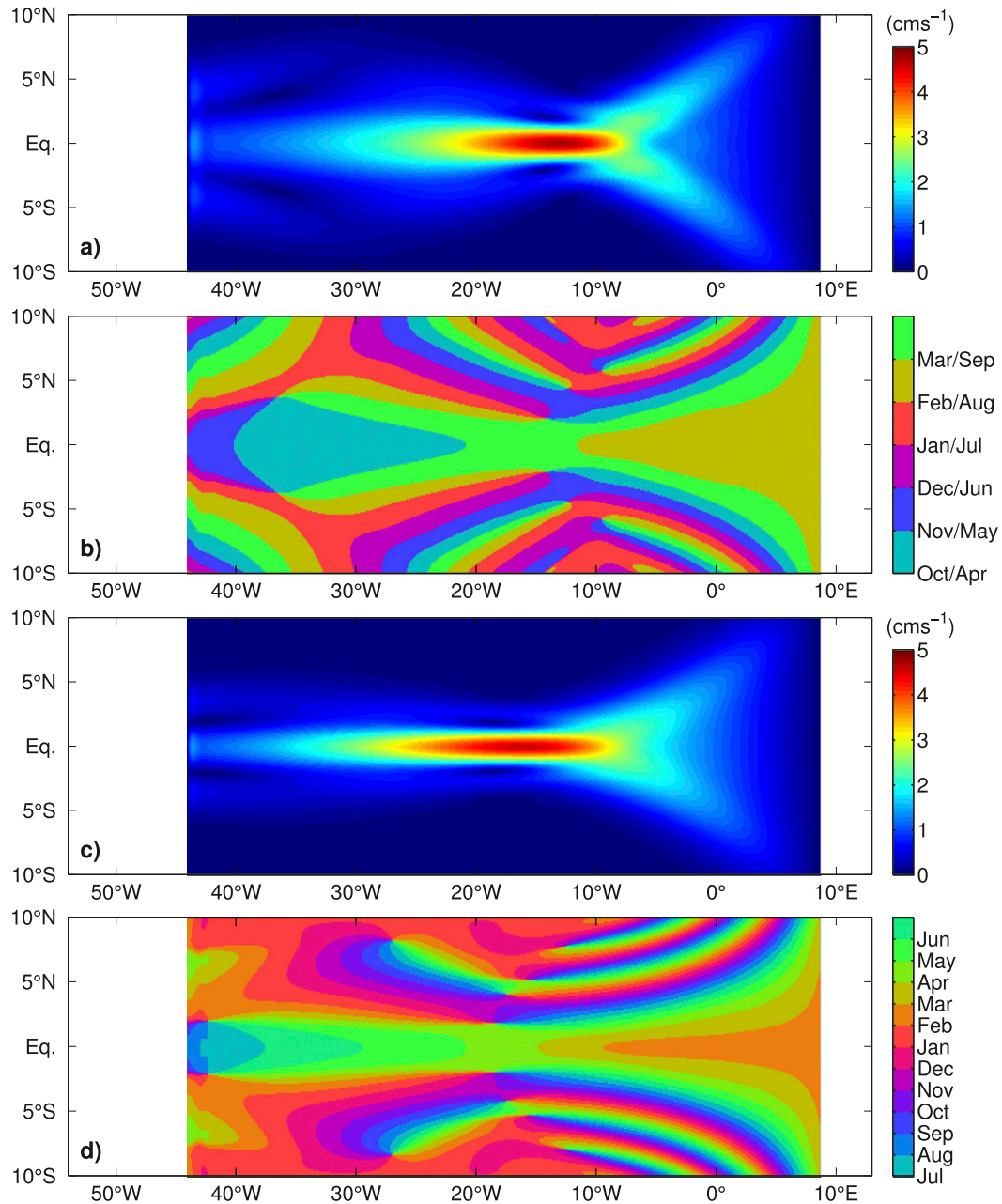


FIG. 8. As in Fig. 6, but simulated with the reduced-gravity model for the rectangular domain using a gravity wave speed $c = 1.32 \text{ m s}^{-1}$ corresponding to the second baroclinic mode and $c = 0.74 \text{ m s}^{-1}$ corresponding to the fourth baroclinic mode.

The comparison of observations with the reconstructed seasonal cycle (Figs. 11a,b,c) shows that (i) at 23°W, the observed EUC transport maximum of the seasonal cycle in September is found only slightly later in the reconstruction; (ii) at 10°W, very good agreement is achieved with EUC transport maximum in August/September, a secondary maximum is in March/April, and the weakest EUC transport is in December; and

(iii) there is only weak or no correspondence between observations and the reconstructions at 0° with the former exhibiting a spring transport maximum, whereas the reconstructions have a weak late boreal summer maximum, similar to what is found in TRATL01 (Fig. 3c). The differences between the three different reduced-gravity model reconstructions, square basin, realistic coastlines, and realistic wind forcing, are relatively

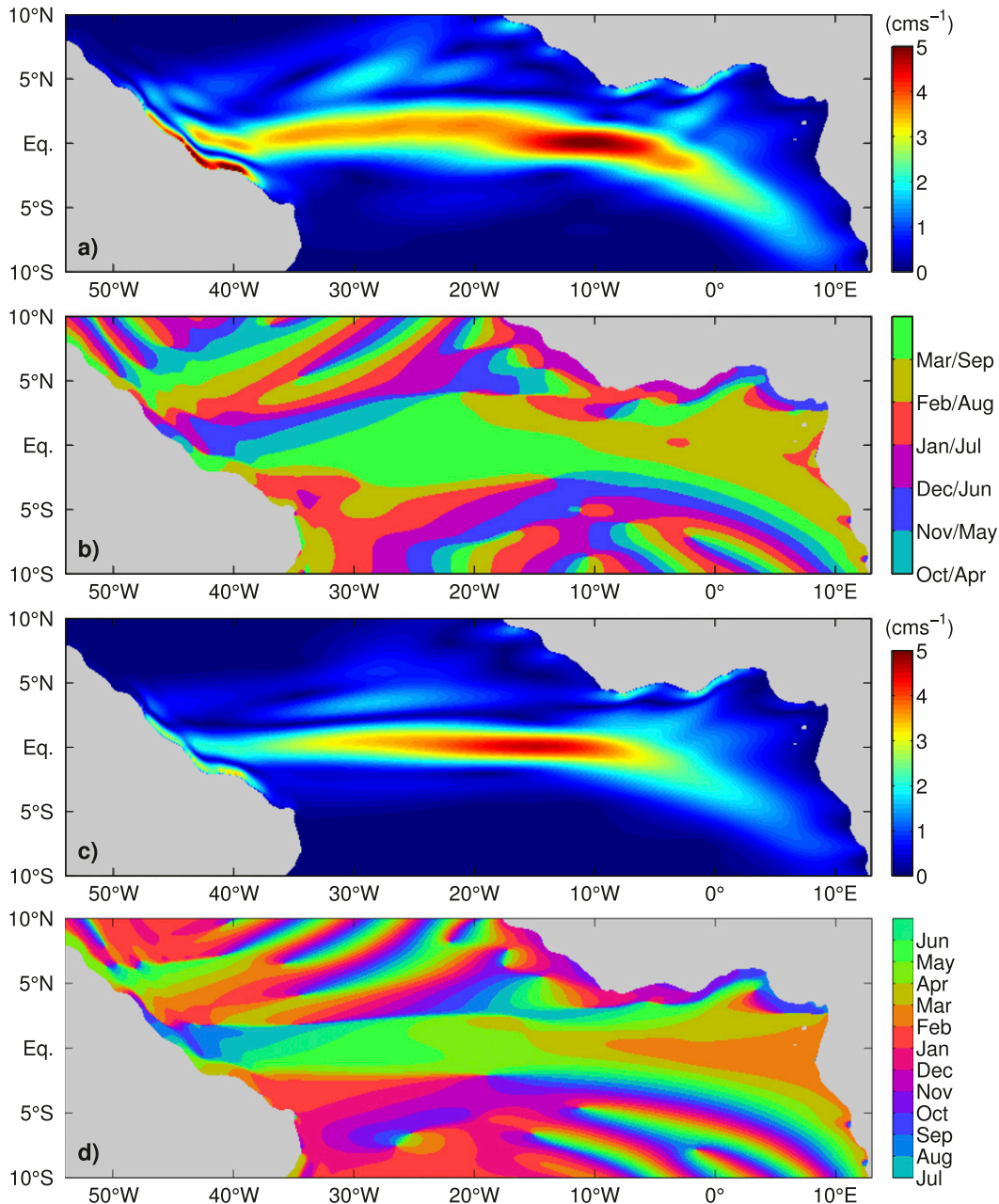


FIG. 9. As in Fig. 8, but for the realistic coastline domain.

small, suggesting robust behavior of the equatorial basin modes. For the reconstructed seasonal cycle of the EUC transport at the three longitudes, the contributions of the annual harmonic cycle and the semiannual harmonic cycle are of similar importance (Figs. 11d,e,f).

To further examine the vertical structure of the seasonal EUC transport variability, zonal transport profiles are calculated by integrating the reconstructed zonal velocity [only eastward velocities following Johns et al. (2014)] over the width of the EUC between 1°12'N and

1°12'S (Fig. 12), which can be directly compared to the observations at 23°W, 10°W, and 0° shown in Johns et al. (2014, their Fig. 11). Here, we also include results regarding the western tropical Atlantic (i.e., 35°W) to analyze the behavior of the EUC across the whole basin. While in general the three different reconstructions are very similar, we note the influence of realistic coastlines compared to the square basin in producing a well-separated and shallower transport maximum at 35°W in boreal spring and a slight weakening of the semiannual

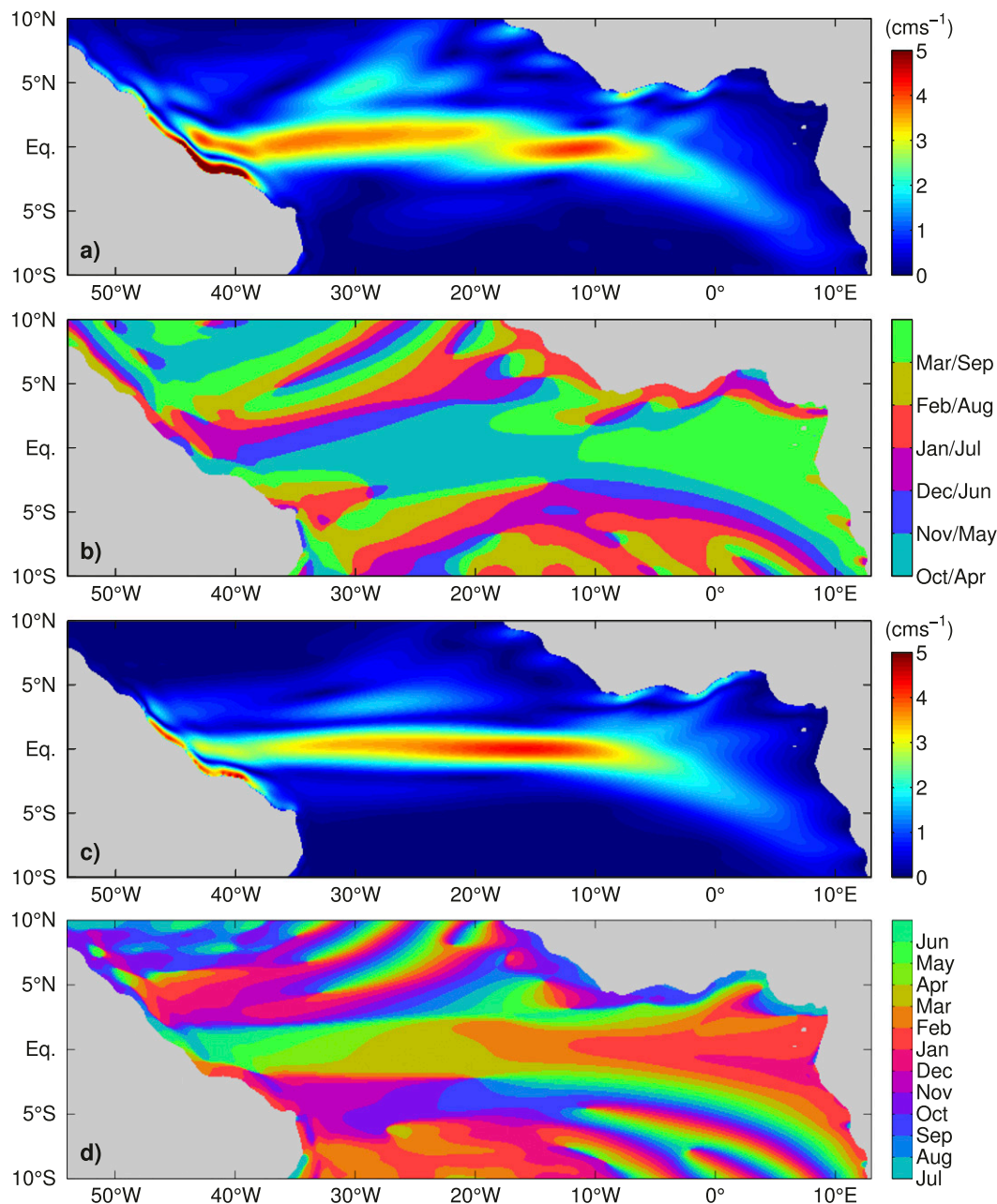


FIG. 10. As in Fig. 9, but with spatially varying forcing.

transport maxima in the eastern equatorial Atlantic when introducing realistic wind forcing. The reconstructed transport profiles obtained by using the second baroclinic mode, semiannual cycle, and the fourth baroclinic mode, annual cycle, show several similarities with the observed total transport profiles (Johns et al. 2014): (i) there is a pronounced semiannual cycle in the shallow part of the transport profile (about upper 100 m), and (ii) the EUC is shallow in boreal spring and deep in boreal autumn. Differences between simulations with the reduced-gravity

model and observations are particularly evident in the flow below the EUC core. In the simulations, it is the deep extension of the EUC during August/September at 0° (Fig. 12) that is chiefly responsible for the EUC transport maximum during that period (Fig. 11c). On the other hand, the observed deep extension of the EUC at 0° is strongest during May shortly after the shallow spring maximum, both together producing the EUC transport maximum in boreal spring (Fig. 11c). The deep extension of the EUC at 10°W and at 23°W

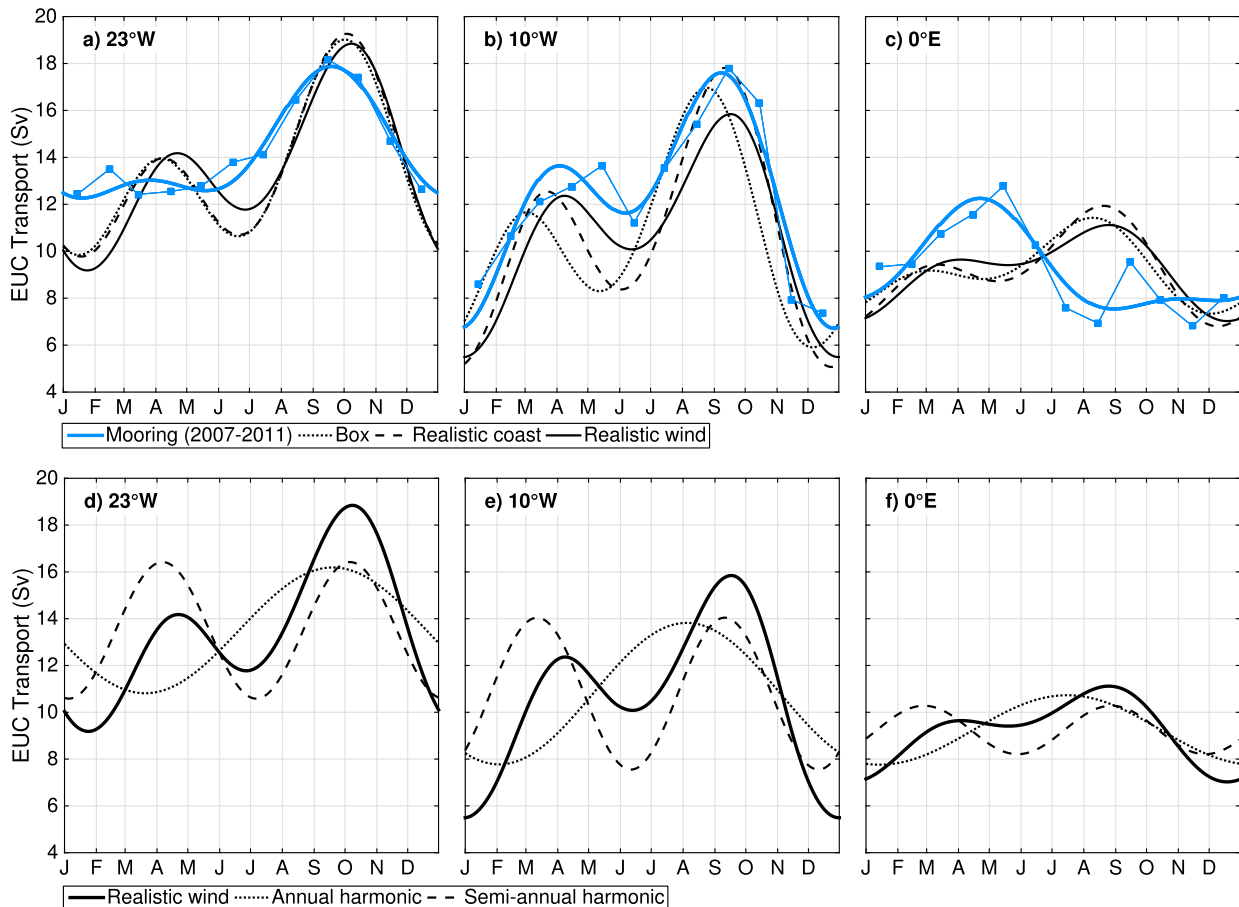


FIG. 11. Monthly means (blue squares, thin blue lines) and annual plus semiannual harmonic cycle of the 30–300-m EUC eastward transport at (a) 23°W, (b) 10°W, and (c) 0° from observations taken from October 2007 to June 2011 (Johns et al. 2014, thick blue lines) and as reconstructed with the three different reduced-gravity model simulations: rectangular domain (dotted lines), realistic coastline domain (dashed lines), and realistic wind forcing (solid lines). The reconstructed annual plus semiannual harmonic cycle for the simulation with realistic wind forcing is repeated in (d), (e), and (f) (solid lines) with separate contributions from the annual harmonic (dotted lines) and semiannual harmonic cycle (dashed lines).

occurs about 1 month later in the simulations compared to the observations.

Other parameters that characterize the seasonal EUC variability are its core depth and latitude as well as its maximum velocity (Fig. 13). These parameters were determined from moored observations at 23°W by Brandt et al. (2014). Comparison of the reduced-gravity model reconstructed fields with the observational curves shows that the semiannual cycle of the EUC core velocity and the annual cycle of the EUC core depth can be largely reproduced by the superposition of the two dominant equatorial basin modes. Even though the vertically averaged annual cycle of the zonal velocity dominates the semiannual cycle (Fig. 5), semiannual variability dominates the annual cycle for the EUC core velocity (Fig. 13b). This is because the second baroclinic mode has a larger amplitude than the fourth baroclinic

mode at the core depth of the mean EUC (Fig. 2). At the same time, the fourth baroclinic mode, annual cycle, very efficiently influences the seasonal cycle of the EUC core depth. With the first zero-crossing of the fourth baroclinic mode at about the core depth of the mean EUC (Fig. 2), the strengthening/weakening above/below the EUC core during boreal spring and vice versa during boreal autumn (Fig. 13d) results in a vertical movement of the EUC core during the annual cycle. The semiannual cycle does not change sign in the depth range of the EUC and thus does not contribute significantly to the vertical movement of the EUC core. The latitude of the EUC core is rather poorly represented by the simple basin modes. Other effects that might play a role in setting this parameter not accounted for in the simulations are the seasonally varying shallow meridional circulation forced by the meridional wind stress on

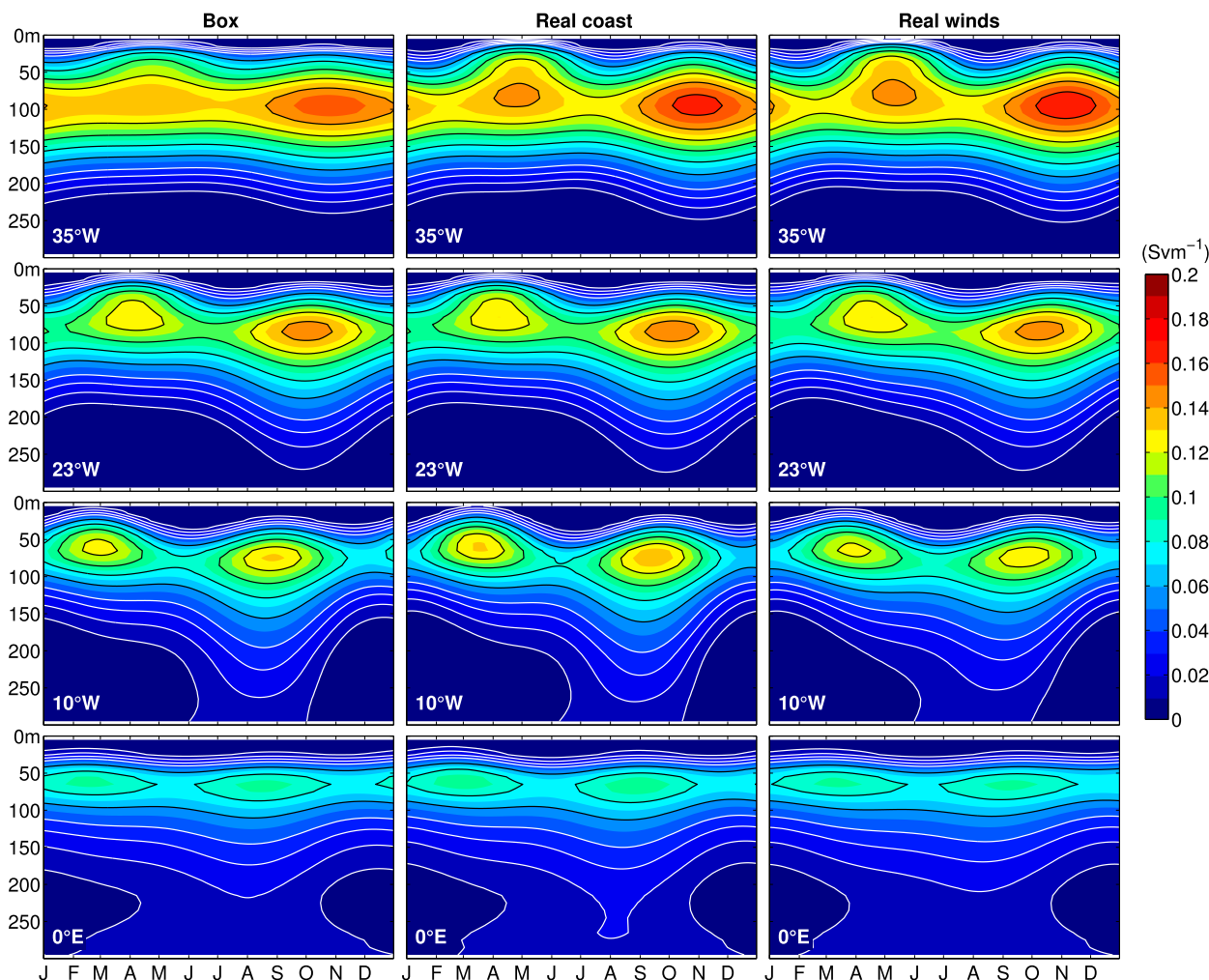


FIG. 12. Monthly mean EUC transport profiles at 35°W, 23°W, 10°W, and 0° for the three different reduced-gravity model simulations: (left) rectangular domain, (middle) realistic coastline domain, and (right) realistic wind forcing. White contour lines are included for transports between 0.01 and 0.04 Sv m^{-1} ($1 \text{ Sv} = 10^6 \text{ m}^3 \text{ s}^{-1}$) with an increment of 0.01 Sv m^{-1} and black lines between 0.06 and 0.2 Sv m^{-1} with an increment of 0.02 Sv m^{-1} .

the equator and the quasi-stationary meandering of the EUC east of the North Brazil Current retroflection, likely responding to the strong seasonal cycle of the retroflection.

5. Summary and discussion

We have analyzed a multiyear velocity time series from the equator, 23°W, covering (with some gaps; see Fig. 1) the whole water column with respect to the seasonal variations of the zonal velocity. Distinct peaks in frequency baroclinic mode space emerged, the most pronounced being the second baroclinic mode at the semiannual period and the fourth baroclinic mode at the annual period (Fig. 5). Similar peaks are found in the TRATL01 simulation. The associated horizontal

patterns as obtained from the TRATL01 model are consistent with the presence of equatorial basin modes, as confirmed using a linear, reduced-gravity model (Figs. 7–10). The general agreement in the horizontal pattern as obtained from TRATL01 and the different runs with the reduced-gravity model also suggest that other effects not accounted for in the reduced-gravity model, such as the seasonal variability in the stratification associated with a vertical displacement of the mean zonal velocity profile, play only a minor role in producing zonal velocity anomalies of the specific baroclinic mode analyzed here.

By using a linear, reduced-gravity model for the simulation of equatorial basin modes for two different baroclinic modes, we were able to show that linear wave dynamics provide a simple explanation for several

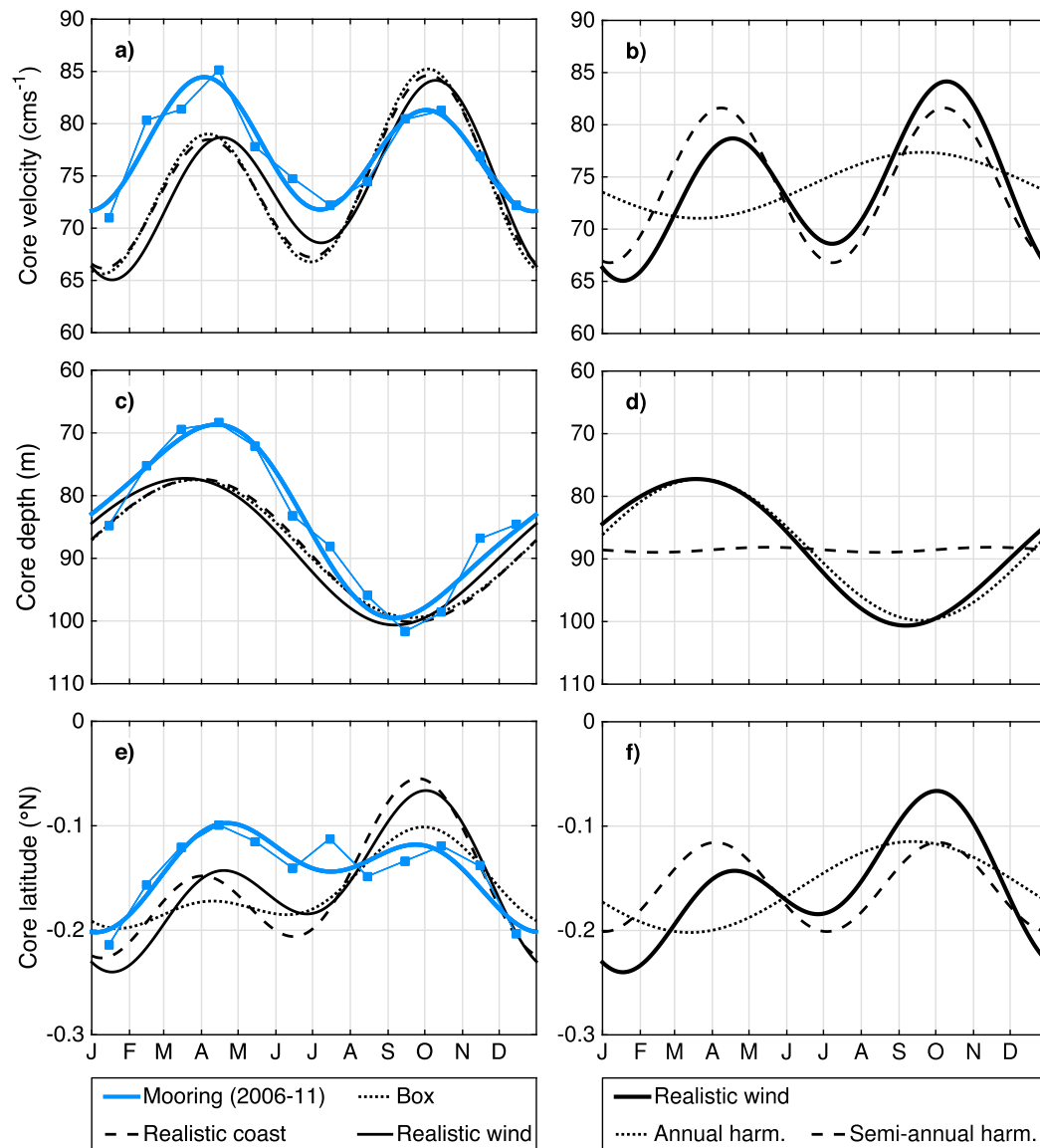


FIG. 13. Monthly means (blue squares, thin blue lines) and annual plus semiannual harmonic cycle of the (a) EUC core velocity, (c) EUC core depth, and (e) EUC core latitude at 23°W from observations taken from June 2006 to June 2011 (Brandt et al. 2014, thick blue lines) and as reconstructed with the three different reduced-gravity model simulations: rectangular domain (dotted lines), realistic coastline domain (dashed lines), and realistic wind forcing (solid lines). The reconstructed annual plus semiannual harmonic cycle for the simulation with realistic wind forcing is repeated in (b), (d), and (f) (solid lines) with separate contributions from the annual harmonic (dotted lines) and semiannual harmonic cycle (dashed lines).

characteristics of the observed zonal velocity seasonal variability including that of the EUC. Besides equatorial beams that are often used to describe the seasonal variability in the equatorial ocean (McCreary 1984; Lukas and Firing 1985; Thierry et al. 2004; Brandt and Eden 2005), equatorial basin modes represent a powerful alternative means of describing equatorial ocean dynamics (Cane and Moore 1981; Jensen 1993; Han et al. 1999;

Ding et al. 2009; Han et al. 2011). Equatorial basin modes are associated with basin resonances occurring at periods defined by the phase speeds of equatorial Kelvin and long Rossby waves of specific baroclinic modes and the basin geometry. In conjunction with the characteristics of the wind forcing, basin resonance appears to explain the pronounced peaks in the frequency baroclinic mode space found in the moored observations.

The simulations with the reduced-gravity model in different configurations and the TRATL01 model confirm the result obtained by [Han et al. \(2011\)](#) and others that the resonant equatorial basin modes are robust features only weakly dependent on the structure of the equatorial basin and the wind forcing. [Thierry et al. \(2004\)](#) specifically analyzed the role of the Mid-Atlantic Ridge and found a negligible effect of this pronounced bathymetric feature, suggesting that a simple reduced-gravity model might be well suited for the simulation of equatorial basin modes.

While the resonance of the semiannual cycle in the Atlantic (as well as Indian) Ocean requires a phase speed close to the phase speed of the second baroclinic mode ([Thierry et al. 2004](#); [Ding et al. 2009](#)), the resonance of the annual cycle is associated with a slower internal wave speed, which is achieved in the equatorial Atlantic by the fourth baroclinic mode. The higher baroclinic mode has a first zero-crossing of the associated vertical structure function (derived from observations) at about 65-m depth ([Table 1](#)), suggesting an opposing effect of the annual basin mode on the zonal flow above and below the mean EUC core, as seen in the observations ([Fig. 4a](#)).

The seasonal cycle of the EUC reveals strong deviations from a simple local response to the wind forcing. Such deviation can be seen, for example, by the following: (i) the basinwide vertical migration of the EUC within the seasonal cycle cannot be in balance with the differing wind forcing in the eastern (predominantly semiannual forcing) and western (predominantly annual forcing) basin at the same time, and (ii) the maximum of the EUC core velocity during boreal spring is found during the period of weakest wind forcing ([Johns et al. 2014](#)). Using the reduced-gravity model simulations, we show that the superposition of the two dominant basin modes, that is, the second baroclinic mode, semiannual cycle, and the fourth baroclinic mode, annual cycle, provide a simple explanation for a substantial part of the observed seasonal EUC variability. Particularly, the seasonal cycles of the EUC transport, core depth, and core velocity in the central equatorial Atlantic are well captured by the reconstructed velocity fields. However, the superposition of the two basin-mode solutions cannot account for the downward phase propagation of the annual cycle found below the EUC core ([Fig. 4](#)), which must involve other baroclinic modes ([Brandt and Eden 2005](#)). This discrepancy between the simulations and observations is probably responsible for the deviations in the transport profiles derived from the reconstructions ([Fig. 12](#)) and observations ([Johns et al. 2014](#)). It might also be the reason that although the amplitudes of the two basin modes are adjusted in comparison to the

23°W velocity data, the reconstructed and observed EUC transport at 23°W does not completely match ([Fig. 11a](#)).

There is general disagreement between observations and the linear reduced-gravity model simulations as well as GCM simulations of the EUC in the eastern equatorial Atlantic, for example, at 0°. [Philander and Chao \(1991\)](#) suggested that in the eastern equatorial Atlantic, the EUC acts as an inertial jet decelerated by lateral dissipation. As shown in satellite ([Athie and Marin 2008](#)) and in situ observations ([Jouanno et al. 2013](#)), there is a strong seasonal cycle of the amplitude of intraseasonal waves. Model simulations indicate that these waves, which are mainly wind generated by the high-frequency wind forcing, impact the seasonal cycle of turbulent mixing in the eastern equatorial Atlantic ([Jouanno et al. 2013](#)). Through their effects on lateral dissipation and vertical mixing, the intraseasonal variability might influence the seasonal cycle of the zonal velocity in the eastern equatorial Atlantic. However, such effects might also play a role in the central equatorial Atlantic, which is also characterized by substantial seasonal cycles in the strengths of tropical instability waves ([Athie and Marin 2008](#)) and vertical mixing ([Jouanno et al. 2011](#); [Hummels et al. 2014](#)). These effects are not captured in the reduced-gravity model simulations. Besides the gravest equatorial basin modes discussed so far, we also want to mention a possible role of the second basin modes for the zonal velocity variability in the far eastern equatorial Atlantic. In the case of the fourth baroclinic mode, the second basin mode has substantial oscillation energy at the semiannual period ([Fig. 7](#)). The second basin mode likely has a stronger impact on the zonal velocity seasonal cycle east and west of the central equatorial Atlantic, which is dominated by the gravest basin mode. As the second basin mode typically has a reduced amplitude in the central equatorial Atlantic and is thus not well constrained by our observations on the equator at 23°W, it is not included here, but it clearly deserves further study.

To correctly represent the seasonal variability of zonal velocity in GCMs, basin-mode resonance must be captured. As suggested by [Philander and Pacanowski \(1981\)](#), the evaluation of the seasonal cycle provides a sensitivity test of the different mixing parameterizations used in models. However, the response of the reduced-gravity model to varying frequencies of the wind forcing ([Fig. 7](#)) indicates that the amplitude of the annual and semiannual oscillations crucially depends on the proximity of the resonance peaks to the annual and semiannual periods. The resonance periods of the second and fourth baroclinic modes as calculated using the mean

Brunt–Väisälä frequency profile from TRATL01 are 185 and 339 days and as such are about 20 days shorter than the estimates obtained from observations (Table 1). In general, variations in the vertical density structure of GCMs compared to observations could enhance or reduce the wave speeds of the specific baroclinic modes and thus modify the amplitude of the corresponding basin modes by shifting the period of the resonance peaks. Particularly for coarse-resolution models, the vertical density structure could differ substantially from reality. The resulting alteration of the EUC transport seasonal cycle and in turn its associated supply to the equatorial upwelling has great potential to impact simulated sea surface temperature variability.

The analyzed simulation with the TRATL01 model show a deeper EUC (at 23°W; 85 m in TRATL01 vs 70 m in the observations) and a deeper first zero-crossing of the fourth baroclinic mode when using the mean Brunt–Väisälä frequency profile from the model instead from the observations (77 vs 65 m). We also note a shift of the annual cycle to lower modes in the TRATL01 simulation compared to observations (Fig. 5). A similar result can be conjectured from the GCM simulation studied by Ding et al. (2009), where it was found that the model solution is determined by the four gravest baroclinic modes with the second and third being dominant. Simulation of the seasonal cycle of equatorial zonal velocity thus requires, besides valid mixing parameterizations, a realistic representation of the vertical density structure and the mean flow field, both affecting the amplitudes of the annual and semiannual oscillations associated with the resonant basin modes.

Acknowledgments. This study was supported by the Deutsche Forschungsgemeinschaft as part of the Sonderforschungsbereich 754 (SFB754) “Climate–Biogeochemistry Interactions in the Tropical Ocean” and through several research cruises with R/V *Meteor*, R/V *Maria S. Merian*, and R/V *L’Atalante* by the German Federal Ministry of Education and Research as part of the cooperative projects RACE (03F0605B) and SACUS (03G0837A) and by European Union 7th Framework Programme (FP7 2007–13) under Grant Agreement 603521 PREFACE project. Moored velocity observations were acquired in cooperation with the PIRATA project, with additional support for the moored profiler observations provided by the U.S. National Science Foundation. We thank the captains and crew of the R/V *Maria S. Merian*, R/V *Meteor*, and R/V *L’Atalante* as well as our technical group for their help with the fieldwork. TRATL01 has been developed by F. U. Schwarzkopf and the Kiel ocean modelling group as part of the European DRAKKAR collaboration. The

model simulations were performed at the North-German Supercomputing Alliance (HLRN). NCEP–DOE AMIP-II Reanalysis data were provided by the NOAA/OAR/ESRL PSD, Boulder, Colorado, United States (<http://www.esrl.noaa.gov/psd/>). The ECMWF ORA-S4 reanalysis data were obtained from ICDC (<ftp://ftp.icdc.zmaw.de/EASYInit/ORA-S4/>).

REFERENCES

- Ascani, F., E. Firing, J. P. McCreary, P. Brandt, and R. J. Greatbatch, 2015: The deep equatorial ocean circulation in wind-forced numerical solutions. *J. Phys. Oceanogr.*, **45**, 1709–1734, doi:10.1175/JPO-D-14-0171.1.
- Athie, G., and F. Marin, 2008: Cross-equatorial structure and temporal modulation of intraseasonal variability at the surface of the tropical Atlantic Ocean. *J. Geophys. Res.*, **113**, C08020, doi:10.1029/2007JC004332.
- Balmaseda, M. A., K. Mogensen, and A. T. Weaver, 2013: Evaluation of the ECMWF ocean reanalysis system ORAS4. *Quart. J. Roy. Meteor. Soc.*, **139**, 1132–1161, doi:10.1002/qj.2063.
- Boyd, J. P., 1980: Equatorial solitary waves. Part I: Rossby solitons. *J. Phys. Oceanogr.*, **10**, 1699–1717, doi:10.1175/1520-0485(1980)010<1699:ESWPIR>2.0.CO;2.
- Brandt, P., and C. Eden, 2005: Annual cycle and interannual variability of the mid-depth tropical Atlantic Ocean. *Deep-Sea Res. I*, **52**, 199–219, doi:10.1016/j.dsr.2004.03.011.
- , F. A. Schott, C. Provost, A. Kartavtseff, V. Hormann, B. Bourles, and J. Fischer, 2006: Circulation in the central equatorial Atlantic: Mean and intraseasonal to seasonal variability. *Geophys. Res. Lett.*, **33**, L07609, doi:10.1029/2005GL025498.
- , A. Funk, V. Hormann, M. Dengler, R. J. Greatbatch, and J. M. Toole, 2011: Interannual atmospheric variability forced by the deep equatorial Atlantic Ocean. *Nature*, **473**, 497–500, doi:10.1038/nature10013.
- , and Coauthors, 2012: Ventilation of the equatorial Atlantic by the equatorial deep jets. *J. Geophys. Res.*, **117**, C12015, doi:10.1029/2012JC008118.
- , A. Funk, A. Tantet, W. Johns, and J. Fischer, 2014: The Equatorial Undercurrent in the central Atlantic and its relation to tropical Atlantic variability. *Climate Dyn.*, **43**, 2985–2997, doi:10.1007/s00382-014-2061-4.
- Cane, M. A., and D. W. Moore, 1981: A note on low-frequency equatorial basin modes. *J. Phys. Oceanogr.*, **11**, 1578–1584, doi:10.1175/1520-0485(1981)011<1578:ANOLFE>2.0.CO;2.
- , and P. R. Gent, 1984: Reflection of low-frequency equatorial waves at arbitrary western boundaries. *J. Mar. Res.*, **42**, 487–502, doi:10.1357/002224084788505988.
- Charney, J. G., 1960: Non-linear theory of a wind-driven homogeneous layer near the equator. *Deep-Sea Res.*, **6**, 303–310, doi:10.1016/0146-6313(59)90089-9.
- Claus, M., R. J. Greatbatch, and P. Brandt, 2014: Influence of the barotropic mean flow on the width and the structure of the Atlantic equatorial deep jets. *J. Phys. Oceanogr.*, **44**, 2485–2497, doi:10.1175/JPO-D-14-0056.1.
- Debreu, L., and E. Blayo, 2008: Two-way embedding algorithms: A review. *Ocean Dyn.*, **58**, 415–428, doi:10.1007/s10236-008-0150-9.
- Ding, H., N. S. Keenlyside, and M. Latif, 2009: Seasonal cycle in the upper equatorial Atlantic Ocean. *J. Geophys. Res.*, **114**, C09016, doi:10.1029/2009JC005418.

- Duteil, O., F. U. Schwarzkopf, C. W. Böning, and A. Oschlies, 2014: Major role of the equatorial current system in setting oxygen levels in the eastern tropical Atlantic Ocean: A high-resolution model study. *Geophys. Res. Lett.*, **41**, 2033–2040, doi:[10.1002/2013GL058888](https://doi.org/10.1002/2013GL058888).
- Fu, L. L., 2007: Intraseasonal variability of the equatorial Indian Ocean observed from sea surface height, wind, and temperature data. *J. Phys. Oceanogr.*, **37**, 188–202, doi:[10.1175/JPO3006.1](https://doi.org/10.1175/JPO3006.1).
- Greatbatch, R. J., 1985: Kelvin wave fronts, Rossby solitary waves and the nonlinear spin-up of the equatorial oceans. *J. Geophys. Res.*, **90**, 9097–9107, doi:[10.1029/JC090iC05p09097](https://doi.org/10.1029/JC090iC05p09097).
- , P. Brandt, M. Claus, S. H. Didwischus, and Y. Fu, 2012: On the width of the equatorial deep jets. *J. Phys. Oceanogr.*, **42**, 1729–1740, doi:[10.1175/JPO-D-11-0238.1](https://doi.org/10.1175/JPO-D-11-0238.1).
- Griffies, S. M., and Coauthors, 2009: Coordinated Ocean-ice Reference Experiments (COREs). *Ocean Modell.*, **26**, 1–46, doi:[10.1016/j.ocemod.2008.08.007](https://doi.org/10.1016/j.ocemod.2008.08.007).
- Han, W. Q., J. P. McCreary, D. L. T. Anderson, and A. J. Mariano, 1999: Dynamics of the eastward surface jets in the equatorial Indian Ocean. *J. Phys. Oceanogr.*, **29**, 2191–2209, doi:[10.1175/1520-0485\(1999\)029<2191:DOTESJ>2.0.CO;2](https://doi.org/10.1175/1520-0485(1999)029<2191:DOTESJ>2.0.CO;2).
- , —, Y. Masumoto, J. Vialard, and B. Duncan, 2011: Basin resonances in the equatorial Indian Ocean. *J. Phys. Oceanogr.*, **41**, 1252–1270, doi:[10.1175/2011JPO4591.1](https://doi.org/10.1175/2011JPO4591.1).
- Hazeleger, W., and P. de Vries, 2003: Fate of the Equatorial Undercurrent in the Atlantic. *Interhemispheric Water Exchange in the Atlantic Ocean*, G. J. Goni and P. Malanotte-Rizzoli, Eds., Elsevier Oceanography Series, Vol. 68, Elsevier, 175–191.
- , —, and Y. Friocourt, 2003: Sources of the Equatorial Undercurrent in the Atlantic in a high-resolution ocean model. *J. Phys. Oceanogr.*, **33**, 677–693, doi:[10.1175/1520-0485\(2003\)33<677:SOTEUI>2.0.CO;2](https://doi.org/10.1175/1520-0485(2003)33<677:SOTEUI>2.0.CO;2).
- Hummels, R., M. Dengler, P. Brandt, and M. Schlundt, 2014: Diapycnal heat flux and mixed layer heat budget within the Atlantic cold tongue. *Climate Dyn.*, **43**, 3179–3199, doi:[10.1007/s00382-014-2339-6](https://doi.org/10.1007/s00382-014-2339-6).
- Jensen, T. G., 1993: Equatorial variability and resonance in a wind-driven Indian-Ocean model. *J. Geophys. Res.*, **98**, 22 533–22 552, doi:[10.1029/93JC02565](https://doi.org/10.1029/93JC02565).
- Johns, W. E., P. Brandt, B. Bourlès, A. Tantet, A. Papapostolou, and A. Houk, 2014: Zonal structure and seasonal variability of the Atlantic Equatorial Undercurrent. *Climate Dyn.*, **43**, 3047–3069, doi:[10.1007/s00382-014-2136-2](https://doi.org/10.1007/s00382-014-2136-2).
- Johnson, G. C., and D. X. Zhang, 2003: Structure of the Atlantic Ocean equatorial deep jets. *J. Phys. Oceanogr.*, **33**, 600–609, doi:[10.1175/1520-0485\(2003\)033<0600:SOTAOE>2.0.CO;2](https://doi.org/10.1175/1520-0485(2003)033<0600:SOTAOE>2.0.CO;2).
- Jouanno, J., F. Marin, Y. du Penhoat, J. Sheinbaum, and J. M. Molines, 2011: Seasonal heat balance in the upper 100 m of the equatorial Atlantic Ocean. *J. Geophys. Res.*, **116**, C09003, doi:[10.1029/2010JC006912](https://doi.org/10.1029/2010JC006912).
- , —, —, and J. M. Molines, 2013: Intraseasonal modulation of the surface cooling in the Gulf of Guinea. *J. Phys. Oceanogr.*, **43**, 382–401, doi:[10.1175/JPO-D-12-053.1](https://doi.org/10.1175/JPO-D-12-053.1).
- Kanamitsu, M., W. Ebisuzaki, J. Woollen, S. K. Yang, J. J. Hnilo, M. Fiorino, and G. L. Potter, 2002: NCEP-DOE AMIP-II Reanalysis (R-2). *Bull. Amer. Meteor. Soc.*, **83**, 1631–1643, doi:[10.1175/BAMS-83-11-1631](https://doi.org/10.1175/BAMS-83-11-1631).
- Lukas, R., and E. Firing, 1985: The annual Rossby wave in the central equatorial Pacific Ocean. *J. Phys. Oceanogr.*, **15**, 55–67, doi:[10.1175/1520-0485\(1985\)015<0055:TARWIT>2.0.CO;2](https://doi.org/10.1175/1520-0485(1985)015<0055:TARWIT>2.0.CO;2).
- Madec, G., 2008: NEMO ocean engine version 3.1. Institut Pierre-Simon Laplace Note du Pole de Modélisation 27, 300 pp.
- McCreary, J. P., 1981: A linear stratified ocean model of the Equatorial Undercurrent. *Philos. Trans. Roy. Soc.*, **A298**, 603–635, doi:[10.1098/rsta.1981.0002](https://doi.org/10.1098/rsta.1981.0002).
- , 1984: Equatorial beams. *J. Mar. Res.*, **42**, 395–430, doi:[10.1357/002224084788502792](https://doi.org/10.1357/002224084788502792).
- Philander, S. G. H., and R. C. Pacanowski, 1981: Response of equatorial oceans to periodic forcing. *J. Geophys. Res.*, **86**, 1903–1916, doi:[10.1029/JC086iC03p01903](https://doi.org/10.1029/JC086iC03p01903).
- , and —, 1986: A model of the seasonal cycle in the tropical Atlantic Ocean. *J. Geophys. Res.*, **91**, 14 192–14 206, doi:[10.1029/JC091iC12p14192](https://doi.org/10.1029/JC091iC12p14192).
- , and Y. Chao, 1991: On the contrast between the seasonal cycles of the equatorial Atlantic and Pacific Oceans. *J. Phys. Oceanogr.*, **21**, 1399–1406, doi:[10.1175/1520-0485\(1991\)021<1399:OTCBTS>2.0.CO;2](https://doi.org/10.1175/1520-0485(1991)021<1399:OTCBTS>2.0.CO;2).
- Qiao, L., and R. H. Weisberg, 1997: The zonal momentum balance of the equatorial undercurrent in the central Pacific. *J. Phys. Oceanogr.*, **27**, 1094–1119, doi:[10.1175/1520-0485\(1997\)027<1094:TZMBOT>2.0.CO;2](https://doi.org/10.1175/1520-0485(1997)027<1094:TZMBOT>2.0.CO;2).
- Schott, F. A., J. P. McCreary, and G. C. Johnson, 2004: Shallow overturning circulations of the tropical–subtropical oceans. *Earth's Climate: The Ocean-Atmosphere Interaction*, *Geophys. Monogr.*, Vol. 147, Amer. Geophys. Union, 261–304.
- , M. Dengler, R. Zantopp, L. Stramma, J. Fischer, and P. Brandt, 2005: The shallow and deep western boundary circulation of the South Atlantic at 5°–11°S. *J. Phys. Oceanogr.*, **35**, 2031–2053, doi:[10.1175/JPO2813.1](https://doi.org/10.1175/JPO2813.1).
- Shankar, D., J. P. McCreary, W. Han, and S. R. Shetye, 1996: Dynamics of the East India Coastal Current: 1. Analytic solutions forced by interior Ekman pumping and local along-shore winds. *J. Geophys. Res.*, **101**, 13 975–13 991, doi:[10.1029/96JC00559](https://doi.org/10.1029/96JC00559).
- Stommel, H., 1960: Wind-drift near the equator. *Deep-Sea Res.*, **6**, 298–302, doi:[10.1016/0146-6313\(59\)90088-7](https://doi.org/10.1016/0146-6313(59)90088-7).
- Thierry, V., A. M. Treguier, and H. Mercier, 2004: Numerical study of the annual and semi-annual fluctuations in the deep equatorial Atlantic Ocean. *Ocean Modell.*, **6**, 1–30, doi:[10.1016/S1463-5003\(02\)00054-9](https://doi.org/10.1016/S1463-5003(02)00054-9).